Numerical Simulation of the Flow About the F-18 HARV at High Angle of Attack

Scott M. Murman

Numerical Simulation of the Flow About the F–18 HARV at High Angle of Attack

Final Report for NASA Grant NCC2–729

Scott M. Murman
Principal Investigator
MCAT Institute, Moffett Field, CA 94035

INTRODUCTION

The flowfield about aircraft maneuvering at high angles of attack is characterized by large regions of separated flow, the formation of strong vortical structures on the leeward side of the aircraft, and a close coupling between the flows about the separate components of the aircraft. As part of NASA's High Alpha Technology Program, research has been aimed at developing and extending numerical methods to accurately predict the high Reynolds number flow about the NASA High Alpha Research Vehicle (HARV) at large angles of attack. The HARV is a highly-instrumented F–18 aircraft which has been used for flight testing because of its exceptional high-angle-of-attack capability. The resulting codes have been validated by comparison of the numerical results with in-flight aerodynamic measurements and flow visualization obtained on the HARV. These flight-validated numerical methods have been used to perform numerical analyses and optimization of new control concepts for high-alpha maneuverability (cf. Ref. 1). This can lead to safer and more efficient aircraft operating at high angles of attack.

This report summarizes research done over the past two years as part of NASA Grant NCC 2-729. This research has been aimed at validating numerical methods for computing the flow about the complete F–18 HARV at $\alpha = 30°$ and $\alpha = 45°$. At 30° angle of attack, the flow about the F–18 is dominated by the formation, and subsequent breakdown, of strong vortices over the wing leading-edge extensions (LEX). As the angle of attack is increased to $\alpha = 45°$, the fuselage forebody of the F–18 contains significant laminar and transitional regions which are not present at $\alpha = 30°$. Further, the flow over the LEX at $\alpha = 45°$ is dominated by an unsteady shedding in time, rather than strong coherent vortices. This complex physics, combined with the complex geometry of a full-aircraft configuration, provides a challenge for current computational fluid dynamics (CFD) techniques. The following sections present a the numerical method and grid generation scheme that was used, a review of prior research done to numerically model the F–18 HARV, and a discussion of the current research. The current research is broken into three main topics; the effect of engine-inlet mass-flow rate on the F–18 vortex breakdown position, the results using a refined F–18 computational model to compute the flow at $\alpha = 30°$ and $\alpha = 45°$, and research done using the simpilified geometry of an ogive-cylinder configuration to investigate the physics of unsteady shear-layer shedding. The last section briefly summarizes the discussion.

1

NUMERICAL METHOD

The numerical simulation process consists of two distinct parts: discretization of the physical space, and numerical integration of the governing equations. For complex geometries such as the F–18 aircraft, a structured multiple-zone scheme or an unstructured grid method is necessary for the discretization. The current work uses a Chimera zonal grid technique.[2] In this method, structured grids are generated about the separate components of the aircraft and then combined to create an overall grid system. The complex physics associated with high-angle-of-attack flowfields mandates using the Navier-Stokes equations. A simpler set of equations, such as the Euler equations, will not accurately capture the details of the massively separated three-dimensional flows. In the current work, the two-factor, implicit F3D code is used because it has been used extensively in the past, and validated for several viscous problems, including high-angle-of-attack flows.

Geometry Definition

The Chimera overset zonal scheme allows considerable flexibility in discretizing the region around the aircraft. The task of grid generation is greatly simplified because the scheme does not require that neighboring grids match along a common surface, rather adjacent grids merely need to overlap each other. Another advantage of using the overset method is that it allows the progressive build-up of a complex geometry by adding grids to model separate components. This can be accomplished without significant modification of existing grids, which would necessitate a grid re-generation. The Chimera approach also allows the numerical method to be varied between zones depending upon the physics encountered (e.g. viscous vs. Euler solvers). The Pegasus code[2] was used to establish the communication between all of the grids. With the grids overlapping, Pegasus determines the best point in mesh A from which to obtain data for a boundary point of mesh B. The code also removes portions of a grid (creates "holes") which are specified as internal to another grid. The grid points which are specified as boundary or hole points are tracked using an integer array i_b, called the iblank value. The iblank value is set to one for field points and zero for the boundary and hole points.

Governing Equations and Numerical Algorithm

For high-Reynolds-number flows, the use of a body-fitted coordinate system allows the full Reynolds-averaged Navier-Stokes equations to be simplified by using the thin-layer approximation.[3] However, in order to treat non-body-conforming grids, and to maintain flexibility in domain decomposition, the thin-layer approximation is extended to all three coordinate directions. The governing equations take the following conservative form

$$\partial_\tau \widehat{Q} + \partial_\xi \widehat{F} + \partial_\eta \widehat{G} + \partial_\zeta \widehat{H} = Re^{-1}(\partial_\zeta \widehat{R} + \partial_\zeta \widehat{S} + \partial_\zeta \widehat{T}) \qquad (1)$$

where $\widehat{Q}$ represents the dependent variable vector, $\widehat{F}$, $\widehat{G}$, and $\widehat{H}$ are the inviscid flux vectors, and $\widehat{R}$, $\widehat{S}$, and $\widehat{T}$ contain the remaining viscous terms. In accordance with the thin-layer approximation $\widehat{R}$, $\widehat{S}$, and $\widehat{T}$ do not contain any cross-derivative terms.

2

The above equations are numerically integrated using the F3D code, an implicit, two-factor scheme that uses central differencing in the η and ζ directions and upwind differencing in the ξ direction. The discretized form of Eq. 1 is

$$\mathcal{L}_f\mathcal{L}_b\Delta\widehat{Q}^{n+1} = -i_b\Delta t\Big\{\delta_\xi^b(\widehat{F}^+)^n + \delta_\xi^f(\widehat{F}^-)^n + \delta_\eta\widehat{G}^n + \delta_\zeta\widehat{H}^n$$
$$-Re^{-1}(\bar{\delta}_\xi\widehat{R}^n + \bar{\delta}_\eta\widehat{S}^n + \bar{\delta}_\zeta\widehat{T}^n) - (D_e|_\eta + D_e|_\zeta)\widehat{Q}^n\Big\} \tag{2}$$

where the forward and backward operators, $\mathcal{L}_f$ and $\mathcal{L}_b$, are given by

$$\mathcal{L}_f = I + i_b\Big\{h\delta_\xi^b(\widehat{A}^+)^n + h\delta_\zeta\widehat{C}^n - hRe^{-1}\bar{\delta}_\zeta J^{-1}\widehat{M}^n J - D_i|_\zeta\Big\}$$

and

$$\mathcal{L}_b = I + i_b\Big\{h\delta_\xi^f(\widehat{A}^-)^n + h\delta_\eta\widehat{B}^n - hRe^{-1}\bar{\delta}_\eta J^{-1}\widehat{N}^n J - D_i|_\eta\Big\}$$

The algorithm can be run in either a non-time-accurate mode, first-order time-accurate mode, or second-order time-accurate mode. In Eq. 2, δ is a three-point second-order-accurate central-difference operator, while $\bar{\delta}$ is a midpoint operator used with the viscous terms. The flux $\widehat{F}$ associated with the ξ direction has been eigensplit allowing the use of backward- and forward-difference operators δ_ξ^b and δ_ξ^f. The matrices $\widehat{A}$, $\widehat{B}$, $\widehat{C}$, $\widehat{M}$, and $\widehat{N}$ result from local linearization of the fluxes about the previous time level. The algorithm outlined above has been shown to be linearly, unconditionally stable. Further details on the development of the algorithm can be found in Refs. 4 and 5.

The only difference between Eq. 2 and the numerical algorithm as applied to a single grid case is the introduction of the integer array i_b which allows the use of overset grids. When $i_b = 1$, Eq. 2 reduces to the original algorithm, while when $i_b = 0$ the right hand side is zero and the scheme reduces to $\widehat{Q}^{n+1} = \widehat{Q}^n$. However, in order to apply most algebraic turbulence models the hole points cannot remain at their initial values. Here, the hole points are filled with data either extrapolated or interpolated from the hole boundaries.

Explicit and implicit numerical dissipation terms (D_e and D_i in Eq. 2) are introduced in the η and ζ directions to suppress the high frequencies associated with central differencing. The implicit smoothing consists of only second-order terms, while the explicit smoothing uses a blend of second- and fourth-order terms. The introduction of i_b in the explicit terms causes the overset scheme to switch from fourth-order to second-order smoothing adjacent to blanked-out regions (cf. Ref. 5).

Turbulence Modeling

In the current work, computations are carried out at high Reynolds number flight conditions. This produces turbulent flow over the majority of the aircraft, with the exception of a small laminar and transitional region near the nose. This region is neglected

3

and the computations are performed assuming the flow to be fully turbulent. The algebraic turbulence model of Baldwin and Lomax[6] is used as the base model throughout the flowfield. This provides a computationally efficient model which has proven to be fairly accurate for attached boundary layer flows.

Because of the massively separated regions encountered at high angles of attack, modifications are required to maintain the integrity of the Baldwin and Lomax model. With the use of a multiple-zone scheme, these modifications can be tailored in different sections of the flowfield depending upon the physics involved. The crossflow separation on the forebody upstream of the LEX is sensitive to the turbulence modeling. Here, the Degani and Schiff[7] crossflow separation modifications were used to limit the models outer-layer search cut-off distance. Over the wing and empennage, a fixed cut-off distance was used to limit the search to remain below the LEX vortices and unsteadiness downstream of the LEX vortex breakdown.

PREVIOUS WORK

Figure 1 shows the F–18 HARV during flight tests at the NASA Dryden Flight Research Facility. The geometry is very complex consisting of a swept wing with sharp leading-edge extensions (LEX), an engine-inlet boundary layer diverter and vent, and a wing-leading-edge flap and horizontal tail which are scheduled with angle of attack. Rather than attempt to model the entire aircraft in the first step, the model of the F–18 HARV was progressively built-up so that each new model added more of the details of the geometry. This progression included solutions obtained for the isolated fuselage forebody and LEX,[8] the forebody/LEX and wing,[9] the forebody/LEX and wing with deflected flap,[10] and a geometry which modeled all of the major components of the HARV geometry.[11] This evolution of computational models is shown in Fig. 2. The computed pressure distribution is compared to the in-flight measurements[12] for these cases in Fig. 3. The pressure-port locations on the F–18 HARV are shown in Fig. 4. It can be seen that once the wing is added the surface pressure distribution on the forebody is in good agreement with the flight data at all stations. The complete geometry does show a slightly stronger LEX primary vortex suction peak at fuselage station (F.S.) 253 compared to the simplified geometry configuration. In this case the LEX vortex breakdown position moves upstream relative to the simplified geometry and is in closer agreement with the breakdown position visualized in-flight. The simplified geometry appears to give a better correlation with the flight data than the full geometry at the last two LEX pressure tap stations (F.S. 296 and F.S. 357). This is misleading, and is due to the vortex not dissipating prior to breakdown in the simplified geometry computation, causing the LEX primary vortex suction peak to remain high.

COUPLED EXTERNAL AND ENGINE-INLET FLOW

At moderate-to-high angles of attack the vortices shed from the wing leading-edge extensions (LEX) on the F–18 become unstable, eventually leading to vortex breakdown. This vortex phenomenon is important from both an aerodynamic standpoint as it causes unsteady loadings, and structurally as it can lead to fatigue due to tail buffeting. Flight

4

tests using the F–18 HARV have shown that engine inlet flow has a strong effect on the vortical structure above the LEX.[13] Specifically, as the flow through the inlets increases, as with increasing thrust, the vortex breakdown location moves downstream. Physically, the external and internal flows are closely linked. The objective of this work was to numerically simulate the coupled external and engine inlet flows, at actual flight operating conditions, of the F–18 at high angles of attack.

Geometry Definition

Figure 5 shows a representation of the F–18 surface geometry in the region of the engine inlets. The geometry is quite complex, consisting of a boundary layer diverter vent and splitter plate, along with a highly concave nacelle-wing junction. As with the strategy in creating the grids for the overall aircraft geometry, the complete details of the inlet region were not modeled in the first step, rather a simplified model of the inlet region was developed to investigate the main effect of engine-inlet flow on the external flowfield. The previous model of the F–18 HARV had a fairing covering the inlet region (Fig. 2). A representation of the engine diffuser obtained from CAD data was allowed to expand so that at the duct entry it completely covered the existing inlet fairing. This cross section was then extrapolated upstream to remove the portion of the fairing ahead of the duct entry. In effect, this surface defines the side of the fuselage and lower surface of the LEX upstream of the duct entry, and the internal diffuser downstream of the duct entry (Fig. 6). The distortion of the diffuser to remove the faired-over geometry will alter the flowfield in this area. However, with the use of a mass flow rate boundary condition in the diffuser, and a geometrically similar duct entry, the capture area of the engine should be approximately the same as if the geometry were unaltered. Thus, the effect on the remainder of the external flowfield should be reasonably accurate even though the details of the inlet region geometry are not accurately resolved. In order to resolve the details at the entry to the inlet, an additional grid was created to model the cowling. This grid wraps around the external fuselage into the internal diffuser (Fig. 7). Clustering was specified both normal to the solid surface, and at the lip of the cowling.

The inlet duct uses a mass flow rate boundary condition to simulate engine performance. The diffuser grid extends downstream from the inlet entry to the engine compressor face. Downstream of the compressor face a converging-diverging nozzle is added to the diffuser (Fig. 6). The throat area of this section is chosen so that the flow will choke, and thus control the mass flow rate through the entire duct. In this manner, different engine power settings can be simulated by simply opening or constricting the throat of the nozzle. Since the flow is choked at the throat, a uniform pressure can be imposed at the downstream exit of the diverging nozzle with the only requirement being that $p_{exit} < p_{crit}$.

Results and Discussion

The numerical procedure outlined above was used to compute the turbulent flow about the F–18 aircraft at typical high-angle-of-attack flight-test conditions. These conditions correspond to a Mach number of 0.243, a Reynolds number based of mean aerodynamic chord of 10.9×10^6, and an angle of attack of 30.3°. Two engine operating conditions were simulated, corresponding to flight idle and maximum power settings. These condi-

tions were modeled by matching the mass flow rates through the inlet diffuser. The two mass flow rates used were 21 lbm/sec and 63 lbm/sec per engine, for the flight-idle and maximum power settings, respectively. These mass flow rates were obtained from a flight-validated engine performance code, using the above flight conditions.

The computations were performed in a non-time-accurate mode to speed up convergence. Flight-test visualizations and computations both indicate that the flow is steady ahead of the LEX vortex breakdown location. However, the vortex breakdown location and the flow structure downstream of the breakdown is highly unsteady. The unsteadiness in the computed vortex flowfield resulted in an axial oscillation of the breakdown location with time. The flow visualizations were chosen to best represent the mean computed location of the breakdown, allowing that the computations were not performed in a time-accurate mode.

Figure 8 shows the computed streaklines obtained by releasing particles into the flowfield just upstream of the apex of the LEX. The three cases shown are the faired-over inlet configuration (Fig. 8a), the flight-idle engine setting (Fig. 8b), and the maximum power engine setting (Fig. 8c). The tight vortical flow structure over the LEX breaks down, or bursts, above the wing as indicated by the sudden expansion of the particle traces. There is a downstream movement of the burst location with increasing inlet mass flow rate. This can most easily be seen by comparing Figs. 8a and 8c, where the burst point for the faired-over inlet is upstream of the wing leading edge, while for the maximum power case it is aft of the leading edge. A downstream movement of the vortex breakdown location with increasing engine mass flow rate has been observed in flight tests. Smoke flow visualizations on the HARV aircraft at 25° angle of attack,[14] for idle and maximum power settings, are shown in Fig. 9. The downstream movement of the vortex breakdown location with increasing thrust is clearly visible.

The primary cause of the movement of the LEX vortex breakdown location shown in Fig. 8 is the change in the axial and rotational momenta of the vortex due to "spillage effects" from the flow beneath the LEX. The flowfield beneath the LEX is strongly affected by changes in the inlet mass flow rate. This can be seen in the computed surface flow patterns shown in Fig. 10. When the inlet is faired over (Fig. 10a), the flow on the side of the fuselage under the LEX reverses and is convected outboard over the leading edge of the LEX (Fig. 10a). This behavior has two effects on the LEX vortex: it reduces the axial momentum of the vortex due to interactions with the low momentum reversed flow, and it increases the rotational momentum of the vortex due to the increased outboard flow around the LEX. Both of these effects will tend to promote an earlier vortex core breakdown. In the flight-idle configuration (Fig. 10b), the extent of the reversed flow region is reduced. Part of the flow enters the inlet, while the remainder is convected around the LEX just upstream of the duct entry (Fig. 10b). The reduction of the low axial momentum flow around the LEX reduces the adverse pressure gradient the LEX vortex must overcome. The amount of outboard flow around the LEX is also less than in the faired-inlet configuration. Both of these effects will tend to delay the onset of vortex breakdown. In the maximum power configuration (Fig. 10c), all of the surface streamlines under the LEX enter the inlet. In this case the same arguments apply, and the vortex breakdown is located furthest aft.

6

Similar changes in flow structure under the LEX with increasing inlet mass flow rate have also been observed in sub-scale water-tunnel experiments.[15]

As mentioned above, the computations were all carried out in a non-time-accurate mode to increase the convergence rate, although the physics involved is inherently unsteady. In order to assess the effect this had on the solutions, the above faired-inlet computation was continued in both a non-time-accurate and time-accurate mode. The LEX vortex breakdown position was computed within the code at each time-step, and is shown for both computations in Fig. 11. It can be seen that the two cases follow the same path for a few iterations, and then the time-accurate computation diverges. The vortex breakdown position moves upstream relative to the non-time-accurate computation and is in closer agreement with the position visualized during flight-tests. From this behavior, it was determined that all future computations will only use the time-accurate, or constant time-step, mode.

Summary

Coupled Navier-Stokes simulations of the external and engine inlet flows for the F-18 aircraft were successfully computed for high-angle-of-attack flight-test conditions. These computations were used to investigate the effects of actual engine operating conditions on the external flowfield. The results indicate a strong coupling of the external and inlet flows, especially at the maximum power engine setting. Increasing the mass flow rate through the inlets caused the LEX vortex breakdown location to move progressively downstream. This is consistent with trends observed in flight tests performed on the F-18 HARV. A reversed flow region upstream of the inlet duct is visible in the faired-inlet and flight-idle configurations. This flow reversal is reduced in the flight-idle setting, and is no longer present at the maximum power setting. The large-scale changes in flow feature at the maximum power setting highlight the importance of simulating engine performance in high-angle-of-attack aircraft computations.

F-18 COMPUTATIONS THROUGH $\alpha = 45°$

The majority of the previous numerical analysis and comparison with in-flight measurements has been carried out at angles of attack ranging up to 30°. At these angles of attack, the flowfield about the F-18 is dominated by the formation, and subsequent breakdown, of strong vortices over the wing leading-edge extensions. The computations provided a good qualitative analysis of the flowfield, but showed that a greater grid resolution was required to provide accurate quantitative data in the region of the LEX vortex. The following work used a grid sensitivity study to determine the requirements necessary to accurately resolve both the induced viscous boundary layers and the inviscid vortical structures which form on the leeward side of the F-18 at high angles of attack. In this investigation, the features of the previous computational models were also incorporated into a new model of the F-18 HARV, and the numerical validation was extended to 45° angle of attack.

Geometry Definition

The current grid system is an evolution of the geometry presented in the previous section (also cf. Ref. 16). In that work, a simplified approximation for the inlet duct was added to an existing external grid system, and the internal engine inlet flow was coupled with the external flowfield. The current work extended this coupling by modeling the actual engine diffuser geometry, as well as the boundary layer diverter plate and vent. An overview of the grid system is shown in Fig. 12. The fuselage is broken into two halves, fore and aft, and a sting grid is attached to the aft end of the aircraft. Using the Chimera grid method, the aft fuselage grid is coupled with grids modeling the wing and deflected leading-edge flap, and the horizontal and vertical tails. In addition, an inviscid mesh (not shown) surrounds the complete viscous grid system.

Figure 13 shows a close-up view of the engine inlet region. As mentioned above, all of the components of the inlet boundary layer diverter geometry are modeled. In order to model the actual inlet geometry and obtain the correct engine capture area, the details of the components surrounding the inlet were also needed. This was necessary to incorporate the duct within the existing external grid system using the Chimera method. The mass-flow-rate exit boundary condition reported in the last section were used at the exit plane of the inlet diffuser grid to simulate actual engine operating conditions. The engine operating conditions used were again obtained from a flight-validated engine performance code used with the HARV.

The flowfield about the F–18 at medium-to-high angles of attack is dominated by the formation of the strong LEX vortices and their subsequent breakdown. Since the use of a full-aircraft configuration to perform grid sensitivity studies is computationally prohibitive, a subset of the fuselage forebody was used to determine the effects of grid spacing on the formation of the forebody and LEX vortices. This subset included the fuselage forebody and LEX region up to the wing (cf. Ref. 17). The effects of near-wall radial spacing, and different circumferential and radial grid densities were investigated. Physically, the isolated fuselage flowfield does not contain large axial gradients and therefore axial-grid-density studies have not been undertaken to date. A similar study of the flow over delta wings[18] indicates that the axial grid spacing is not as significant for strong vortex flows as the circumferential and radial grid densities. The current study was performed at $\alpha = 30°$, since at this angle of attack the LEX vortex breaks down aft of the pressure tap locations on the HARV, and therefore steady flight data exists for comparison. It was felt that a grid system "optimized" for $\alpha = 30°$ would, at the minimum, provide a good starting point for the higher angle of attack cases. The results of this grid sensitivity study highlighted the importance of accurately resolving not only the attached boundary layers on the windward side of the body, but the induced boundary layers on the leeward side of the body. The final fuselage forebody grid maintained a tighter viscous spacing near the body, along with more points in the circumferential and radial directions. The final grid system for the full aircraft (Fig. 12) consists of 14 zones and 1,705,000 grid points, with 10% of these points being either zonal boundary or hole points.

Results and Discussion

The numerical procedure and grid system outlined above was used to compute the flow about the F-18 aircraft at angles of attack of $\alpha = 30°$ and $45°$. In these computations the flow conditions, including Mach number, Reynolds number, and engine inlet mass flow rate, were chosen to match available flight-test conditions. For the $\alpha = 30°$ case, previous computational simulations are also available, and direct comparisons with the current solutions are made. The $\alpha = 45°$ case was chosen to match data taken at stabilized high-alpha conditions during flight tests of the HARV equipped with thrust vectoring. These tests included flights with natural boundary-layer transition on the forebody, and flights where the boundary-layer transition was forced by transition strips placed longitudinally along the fuselage forebody. The computational conditions are summarized below in Table 1.

Table 1. Computational Conditions

α	M_∞	$Re_{\bar{c}}$	$\dot{m}_e$ (lbm/sec) *
30.3°	0.243	10.9 x 10^6	62.0
44.7°	0.258	9.43 x 10^6	58.0

* Inlet mass flow rate per engine.

Full-Aircraft Solutions at $\alpha = 30°$

Figure 14 shows the computed surface pressure distribution on the fuselage forebody and LEX at axial stations corresponding to the F-18 HARV pressure port locations. The computed results and previous results obtained on a coarser computational grid are compared to the flight-test data.[12] Both computations show a good agreement with the flight data at all stations on the forebody, including the region of the primary forebody vortices which are seen at F.S. 142 and F.S. 184 near the leeward plane of symmetry ($\phi \approx 160°$). The discrepancy at $\phi = 90°$ at F.S. 142 is caused by an antenna fairing on the aircraft which is not modeled in the computation. The current computational results show a markedly improved comparison with the flight measurements in the region of the LEX vortex. At F.S. 253 and F.S. 296, upstream of the LEX vortex breakdown position, the present computational suction peaks are in good agreement with the flight measurements. In contrast, the coarser-grid results do not adequately resolve the primary vortex suction peak. At $\alpha = 30°$, vortex breakdown occurs on the aircraft at a fuselage station of F.S. ≈ 335. This results in the change in the shape of the pressure distribution between that measured at F.S. 296 and that measured at F.S. 357 in the flight data. The present computations indicate that vortex breakdown occurs at F.S. ≈ 375, aft of that observed in the flight testing. Thus, the comparison between computation and flight at F.S. 357 are not in as good agreement. Note that the coarser-grid solutions indicate vortex breakdown occurs at F.S. ≈ 435, even farther aft of the actual breakdown position.

Figure 15 shows the computed surface flow and the flight-test oil-flow[19] patterns on the F-18 forebody and LEX at $\alpha = 30°$. The HARV oil-flow pattern (Fig. 15a) shows the lines of primary and secondary crossflow separation on the fuselage forebody. A primary crossflow separation occurs at the leading edge of the LEX, and the oil flow photo shows and lines of secondary and tertiary separation on the upper surface of the LEX.

9

The current computation (Fig. 15b) shows an improvement in the resolution of the fore-body secondary separation in comparison to that of the coarser-grid solution (Fig. 15c). The finer-grid solution also resolves the details of the secondary and tertiary separation patterns on the leeward side of the LEX. In addition, details of an additional primary and secondary crossflow separation pattern located on the side of the fuselage under the LEX can be seen in the present fine-grid solution. The overall aircraft computed surface flow pattern of the present solution is shown in Fig. 16. Note that in Fig. 16, the flowfield downstream of the vortex breakdown is unsteady, and the computed flow pattern here represents instantaneous surface streaklines.

One of the difficulties encountered in computing flows with vortex breakdown is determining the numerical transient motion of the breakdown position. In the current computation, the breakdown originates near the vertical tail and then progresses upstream to settle into an unsteady oscillation over the LEX. When the breakdown position is determined visually, only a limited subset of the computational run can be processed and a history of breakdown movement is difficult to obtain. A simple method was developed to track the vortex breakdown position each time-step. Outside of the boundary layer, a vector path is created from the minimum value of stagnation pressure at each axial station. This path roughly corresponds to the path of the primary vortex core. When the angle between this path and the local vorticity vector exceeds a critical value, the vortex is said to have broken down. The critical angle used here is 20°, and was determined by inspection of several cases of vortex breakdown, including the previous coarse-grid solution, and studies of flow over delta wings. Figure 17 shows the numerical history of the movement of the vortex breakdown position for the current $\alpha = 30°$ computation. Once the vortex breakdown has established a mean position time histories of the vortex-induced aerodynamic loadings can be computed.

Particle trajectories released from the tip of the forebody and the apex of the LEX in the present computation show the path of forebody and LEX vortices (Fig. 18a). The flight-test smoke flow visualization[19] is shown for comparison (Fig. 18b). The slow expansion of the vortex core upstream of breakdown, and the loss of core structure starting in the vicinity of the LEX-wing junction can be seen. As mentioned previously, the computed vortex breakdown occurs further downstream than is observed in flight. Figure 19 shows the position of the measured[13] and computed vortex breakdown as a function of the angle of attack.

Full–Aircraft Solutions at $\alpha = 45°$

The computed surface pressure distribution on the HARV fuselage forebody, obtained at $\alpha = 45°$ with the current fine-grid system, is compared to available flight-test data[20] in Figure 20. At this angle of attack it was observed in the flight testing that the LEX vortex breakdown position is near the apex of the LEX, and that the flowfield above the LEX is unsteady. As a result, in-flight measurements of the surface pressures on the LEX are not available at this time for comparison. At all stations on the forebody, the computed pressure distributions show good comparison with the flight measurements on the windward side of the body where the boundary layers remain attached. However, on

the leeward side of the forebody, some discrepancies are observed. At fuselage stations F.S. 70 and F.S. 85, the computation shows a vortex suction peak at $\phi \approx 135°$ which is not present in the flight-test data. At F.S. 107 the computation shows a strong vortex suction peak, while the flight-test shows that a similar vortex has formed but is located further leeward. At F.S. 142 and F.S. 184, the computation and flight-test data show closer agreement for both the windward and leeward portions of the flowfield.

The current fine-grid system was used to compute the flow about the F–18 HARV at 60° angle of attack. The computed results for this case again showed good agreement for the windward-side attached boundary layers, however, on the leeward side of the fuselage forebody a numerical unsteadiness was observed. A high frequency vortex shedding in both time and space was visible in the $\phi = 90° - 135°$ region at all stations on the forebody. It was felt that this was a numerical problem, rather than a physical phenomena, which was being caused by the grid system. Specifically, the circumferential grid clustering used to model the LEX was appearing to cause an instability at this angle of attack. In order to better understand the cause of the high frequency oscillations that appeared on the leeward side of the forebody at $\alpha = 60°$, and to pursue an improved correlation with the flight-test data at $\alpha = 45°$, a new grid system was created which models the forebody and LEX regions separately. The LEX grid was maintained as before, and a limited grid sensitivity study was performed on an isolated forebody nose at $\alpha = 60°$. From this study, a grid for the nose of the forebody was generated having 28 axial, 123 circumferential, and 98 radial points. The use of 28 axial points corresponds to a doubling of the axial grid resolution on the nose. Instead of clustering in the circumferential direction near $\phi = 90°$, a smoother circumferential grid spacing was used with a slight clustering towards the leeward symmetry plane. The surface grid line distribution for the modified two-zone fuselage forebody grid system is shown in Fig. 21, and compared to the original one-zone fine grid. In Fig. 21 only every other circumferential grid line is shown for clarity.

The modified grid system using separate components for the nose and LEX regions was used to re-compute the flowfield at $\alpha = 45°$. The computed surface pressure distribution obtained on the original fine grid and the modified fine-grid system are compared to the flight-test data in Fig. 22. The modified-grid solution shows a better correlation with the flight data at all stations. At F.S. 70 and F.S. 85, the new grid shows a smaller primary vortex has formed which is located closer to the leeward symmetry plane than in the previous computation. At F.S. 107, the strong primary vortex suction peak at $\phi \approx 160°$ is more sharply defined and in closer agreement with the flight-test pressure measurements. Also, the pressure distribution near the leeward symmetry plane shows a much better correlation with the flight data. At F.S. 142, strong suction peaks caused by the primary and secondary forebody vortices are visible at $\phi = 160°$ and $\phi = 140°$, respectively. This pattern is visible but slightly smeared in the original computation. The secondary vortex suction peak is not visible in the flight-test data obtained with either natural transition on the forebody, or forced transition using the fuselage grit strips. As mentioned earlier, the discrepancy observed at $\phi = 90°$ is due to an antenna fairing on the aircraft which is not modeled in the computations. At F.S. 184, the agreement between the solution obtained with the updated grid system and the flight-test data is good.

11

In general, the computed results obtained with the modified two-zone forebody grid show better agreement with the flight measurements. However, at F.S. 107 for $90° \leq \phi \leq 130°$, the pressures obtained with both grids are in close agreement, but are only in fair agreement with the flight measurements. This is believed to be due to the computational assumption of a fully turbulent flow on the aircraft. As mentioned, at 45° angle of attack the flow on the HARV forebody includes a laminar and transitional region which extends approximately 4 feet aft of the nose (see Fig. 12 of Ref. 23). The transition strips which were applied to forebody of the HARV reduce this region (see Fig. 22), but do not remove it altogether. Note that at the downstream stations, where the actual flow is more fully turbulent and the laminar and transitional region near the nose has less effect, the correlation between the fully-turbulent computed results and the flight measurements improves. This points out the need for development of a rational transition model applicable for this class of separated flows.

Summary

Full-aircraft thin-layer Navier-Stokes solutions of the flow about the F–18 HARV were computed at angles of attack $\alpha = 30°$ and 45°. The computations model the relevant geometric features of the F–18 in its high-angle-of-attack configuration, including the wing with deflected leading-edge flap, the empennage, and the details of the engine inlet region and inlet boundary layer diverter. The computations were carried out at flight-test conditions, and were validated against available flight-test data in the form of surface pressure measurements and in-flight flow visualizations. A limited grid sensitivity study was performed on the isolated fuselage forebody and LEX at $\alpha = 30°$ which highlighted the importance of maintaining a suitable grid density not only in the inviscid vortex regions, but also in the vortex-induced viscous boundary layers on the leeward side of the body. The full-aircraft calculations at $\alpha = 30°$ show a good agreement with the flight-test data on the fuselage forebody. At this angle of attack, the computational assumption of a fully turbulent flow is validated. In the LEX region, the present fine-grid solutions show an improved correlation with the flight measurements, over previous coarse-grid results, upstream of the vortex breakdown location. In addition, the computed vortex breakdown position is closer, but still located farther aft than the location visualized during flight tests at this angle of attack. The use of a grid with refined axial spacing in the vortex breakdown region may further improve this correlation.

The computed flowfield at $\alpha = 45°$ was compared to flight-test measurements on the fuselage forebody. In general, the correlation was good, but regions of discrepancy were observed between the computed surface pressure distributions and the flight measurements. The location of the computed LEX vortex breakdown position was in reasonable agreement with that observed in flight. Guided by preliminary computations for $\alpha = 60°$, a modified grid system was generated which used separate grids to model the fuselage forebody nose and LEX regions. Use of these separate grids at $\alpha = 45°$ improved the correlation of the computations with the flight-test data, but discrepancies still remain. Potential sources of the discrepancies are a lack of sufficient grid resolution in the separated flow region, and the computational assumption of fully-turbulent flow on the fuselage forebody while the actual flowfield contains a relatively large region of laminar and transitional flow. These

12

two areas have to be resolved before the flowfield at the extreme angles of attack can be accurately computed.

OGIVE–CYLINDER COMPUTATIONS

The physics of the flow about the HARV changes as the angle of attack is increased from $\alpha = 30°$ to $\alpha = 60°$. At the lower angles of attack, the flowfield is dominated by the formation and subsequent breakdown of the vortices shed from the wing leading-edge extensions (LEX). As the angle of attack increases, the flow about much of the aircraft becomes dominated by an unsteady shedding of the boundary layers, and the convection downstream of these unsteady waves. In order to better understand the physics involved with this unsteady shedding, various computations have been performed using the simpler geometry of a tangent-ogive cylinder at high angle of attack. These computations not only give insight into the physics involved with the full-aircraft geometry, they provide experience and confidence with the numerical code.

Results and Discussion

A variety of cases have been computed for the ogive-cylinder configuration at high angle of attack. This wide variation in computational studies is possible due to the simplified geometry of the ogive-cylinder (Fig. 23). A single-zone grid with approximately 500,000 grid points can provide a highly accurate simulation of the flowfield, as compared to the multi-zone, several million grid point systems that are required to simulate the complete F–18 HARV aircraft. Two body configurations have been computed: one having a 3.5 caliber tangent-ogive portion with a cylinder portion of 7.0 diameters, and the other having a 3.0 caliber tangent-ogive section with a cylinder region extending 12.0 diameters. The study has thus far focused on comparing two angle of attack and Reynolds number combinations, $\alpha = 40°$ and $60°$, and $Re_D = 80,000$ and $200,000$. Both of these Reynolds numbers are assumed to maintain laminar flow throughout the computational region. This combination of different bodies, Reynolds numbers, and angles of attack provides a wide test-bed for the numerical scheme. This test-bed is further extended by also comparing computational cases having a lateral plane of symmetry with the same cases computed using a periodic grid set-up (Fig. 24). These two computational configurations should provide nearly the same results for computations which are symmetric about the lateral plane of symmetry (this includes all cases computed thus far).

$\alpha = 40°$ Computations

The cases that were computed at $\alpha = 40°$ were generally "well behaved," and displayed many of the general features of unsteady boundary layer shedding. Of importance to note were that the computations with the lateral plane of symmetry and the full periodic grid were identical to the order of round-off error, in terms of both the convergence history, and the final median value of normal force. This same behavior was observed in comparing different numerical algorithms. Figure 25 shows the normal force history for an $\alpha = 40°$, $Re_D = 80,000$ case using the 3.0 caliber ogive cylinder body computed using two distinct algorithms. The F3D algorithm uses flux-vector splitting in the streamwise direction while the Beam and Warming algorithm (B&W) uses a central differencing scheme in

13

the streamwise direction with added numerical dissipation. As can be seen from the force history, both algorithms are showing nearly identical behavior at this angle of attack and Reynolds number.

Two cases were computed using the same ogive-cylinder body at 40° angle of attack, with different Reynolds number, $Re_D = 80,000$ and $200,000$. This shows the difference in shedding frequency and amplitude of the pressure variations as the Reynolds number is increased. Figure 26 shows the computed normal force history for the Reynolds number comparison. It is required to compute to a non-dimensional time of near $\hat{t} = 200$ before the initial transients are removed from the computational domain, and a regular periodic variation in normal force is observed. The normal force oscillates at a frequency of approximately 145 Hz in the $Re_D = 80,000$ computation, and 60 Hz in the $Re_D = 200,000$ computation. The amplitude of the oscillation is increased in the $Re_D = 200,000$ computation. The frequency or the normal force variation and the shedding frequency are the same in the $Re_D = 80,000$ computation, however in the $Re_D = 200,000$ computation the two frequencies are not identical. The shedding frequency at $Re_D = 200,000$ is about 4 times as great as the frequency of the normal force oscillation. The cause of this is not known at this time, and further research is planned to understand the behavior. In order to visualize the shedding of the shear layers from the side of the ogive cylinder, an animation of streaklines released in the unsteady flowfield was created using the UFAT visualization program. A snapshot of this animation is shown is Fig. 27. The shedding waves are clearly visible as the groups of particles, and the convection downstream and rolling into the vortex shed from the nose, can also be seen.

$\alpha = 60°$ Computations

While the cases that were computed at $\alpha = 40°$ were termed well behaved, the computations at $\alpha = 60°$ have thus far been pathologically behaved. However, this is also representative of trends that have been observed in experimental testing, where even small changes in an experimental set-up can lead to large changes in results in the extreme angle of attack range. Where at $\alpha = 40°$ the plane of symmetry and periodic configurations display the same results to the order of round-off error, at $\alpha = 60°$ the two computations show radically dis-similar behavior. Specifically, the lateral force coefficient no longer remains at a nominally zero value in the periodic configuration. This build-up of lateral force influences the other force and moment coefficients to diverge from their "symmetric" values as well. This behavior is not consistent between algorithms, as can be seen by the history of lateral force coefficient shown in Fig. 28. Here, both the F3D and Beam and Warming algorithms show a build-up in lateral force, but the mean values and amplitudes of motion are different. In fact, the side forces seen in the two computations are of opposite sign. This behavior has been extensively investigated in order to better understand how a nominally symmetric algorithm can generate asymmetric solutions. Progress has been made, however any results which could be stated now would be conjecture.

REPORT SUMMARY

Full-aircraft thin-layer Navier-Stokes solutions of the flow about the F–18 HARV were computed at angles of attack $\alpha = 30°$ and $\alpha = 45°$. The computations model the

relevant geometric features of the F-18 in its high-angle-of-attack configuration, including the wing with deflected leading-edge flap, the empennage, and the engine inlet region. The computations were carried out at flight-test conditions, and were validated against available flight-test data in the form of surface pressure measurements and in-flight flow visualizations. The computations indicate a strong coupling of the external and engine inlet flows, especially at the maximum power engine setting, which highlights the importance of simulating engine performance in high-angle-of-attack computations. The full-aircraft calculations at $\alpha = 30°$ show a good agreement with the flight-test data in both qualitative and quantitative aspects. The assumption of a fully turbulent flowfield is validated at this angle of attack. The computed flowfield at $\alpha = 45°$ shows a good correlation with the flight-test data available on the fuselage forebody, although the agreement is not as favorable as at $\alpha = 30°$. The significant regions of laminar and transitional flow are the main problem to-date in accurately predicting the flowfield about the F-18 HARV at $\alpha = 45°$. The computational results for ogive-cylinder configurations have highlighted the importance of validating the numerical algorithms before expending resources on full-aircraft solutions at higher angles of attack.

REFERENCES

[1] Gee, K., "Computational Analysis of Forebody Tangential Slot Blowing on the High Alpha Research Vehicle," NASA Grant NCC2-657 Final Report, July 1994.

[2] Benek, J. A., Steger, J. L., Dougherty, F. C., and Buning, P. G., "Chimera: A Grid Embedding Technique," AEDC-TR-85-64, Arnold Air Force Station, TN, 1986.

[3] Steger, J. L., "Implicit Finite-Difference Simulation of Flow About Arbitrary Two-Dimensional Geometries," *AIAA Journal*, Vol. 16, No. 7, 1978, pp. 679-686.

[4] Ying, S. X., Steger, J. L., Schiff, L. B., and Baganoff, D., "Numerical Simulation of Unsteady, Viscous, High-Angle-of-Attack Flows Using a Partially Flux-Split Algorithm," AIAA Paper 86-2179, August 1986.

[5] Buning, P. G., Chiu, I. T., Obayashi, S., Rizk, Y. M., and Steger, J. L., "Numerical Simulation of the Integrated Space Shuttle Vehicle in Ascent," AIAA Paper 88-4359, August 1988.

[6] Baldwin, B. and Lomax, H., "Thin-Layer Approximation and Algebraic Model for Separated Turbulent Flows," AIAA Paper 78-0257, January 1978.

[7] Degani, D. and Schiff, L. B., "Computation of Turbulent Supersonic Flows Around Pointed Bodies Having Crossflow Separation," *Journal of Computational Physics*, Vol. 66, No. 1, September 1986, pp. 173-196.

[8] Schiff, L. B., Cummings, R. M., Sorenson, R. L., and Rizk, Y. M., "Numerical Simulation of High-Incidence Flow over the Isolated F-18 Fuselage Forebody," *Journal of Aircraft*, Vol. 28, No. 10, October 1991, pp. 609-617.

[9] Cummings, R. M., Rizk, Y. M., Schiff, L. B., and Chaderjian, N. M., "Navier-Stokes Predictions for the F-18 Wing and Fuselage at Large Incidence," *Journal of Aircraft*, Vol. 29, No. 4, July - August 1992, pp. 565-574.

[10] Rizk, Y. M., Schiff, L. B., and Gee, K., "Numerical Simulation of the Viscous Flow Around a Simplified F/A–18 at High Angles of Attack," AIAA Paper 90-2999, August 1990.

[11] Rizk, Y. M. and Gee, K., "Numerical Prediction of the Unsteady Flowfield Around the F–18 Aircraft at Large Incidence," AIAA Paper 91-0020, January 1991.

[12] Del Frate, J. H., Fisher, D. F., and Zuniga, F. A., "In-Flight Flow Visualization with Pressure Measurements at Low Speeds on the NASA F–18 High Alpha Research Vehicle," NASA TM-101726, October 1990.

[13] Del Frate, J. H. and Zuniga, F. A., "Off-Surface Flow Visualization, Water Tunnel and Flight," *Proceedings of High-Alpha Technology Program Workshop*, Edwards, CA, November 1989.

[14] Del Frate, J. H., Private correspondence, 1992.

[15] Thompson, D. H., "Water Tunnel Flow Visualization of Vortex Breakdown over the F/A–18," ARL Flight Mechanics Report 179, December 1990.

[16] Murman, S. M., Rizk, Y. M., and Schiff, L. B., "Coupled Numerical Simulation of the External and Engine Inlet Flows for the F–18 at Large Incidence," AIAA Paper 92-2621, June 1992.

[17] Murman, S. M., Schiff, L. B., and Rizk, Y. M., "Numerical Simulation of the Flow about an F–18 Aircraft in the High-Alpha Regime," AIAA Paper 93-3405, August 1993.

[18] Ekaterinaris, J. A. and Schiff, L. B., "Vortical Flows over Delta Wings and Numerical Prediction of Vortex Breakdown," AIAA Paper 90-0102, January 1990.

[19] Fisher, D. F., Del Frate, J. H., and Richwine, D. M., "In-Flight Flow Visualization Characteristics of the NASA F–18 High Alpha Research Vehicle at High Angles of Attack," NASA TM-4193, May 1990.

[20] Fisher, D. F., Private correspondence, 1993.
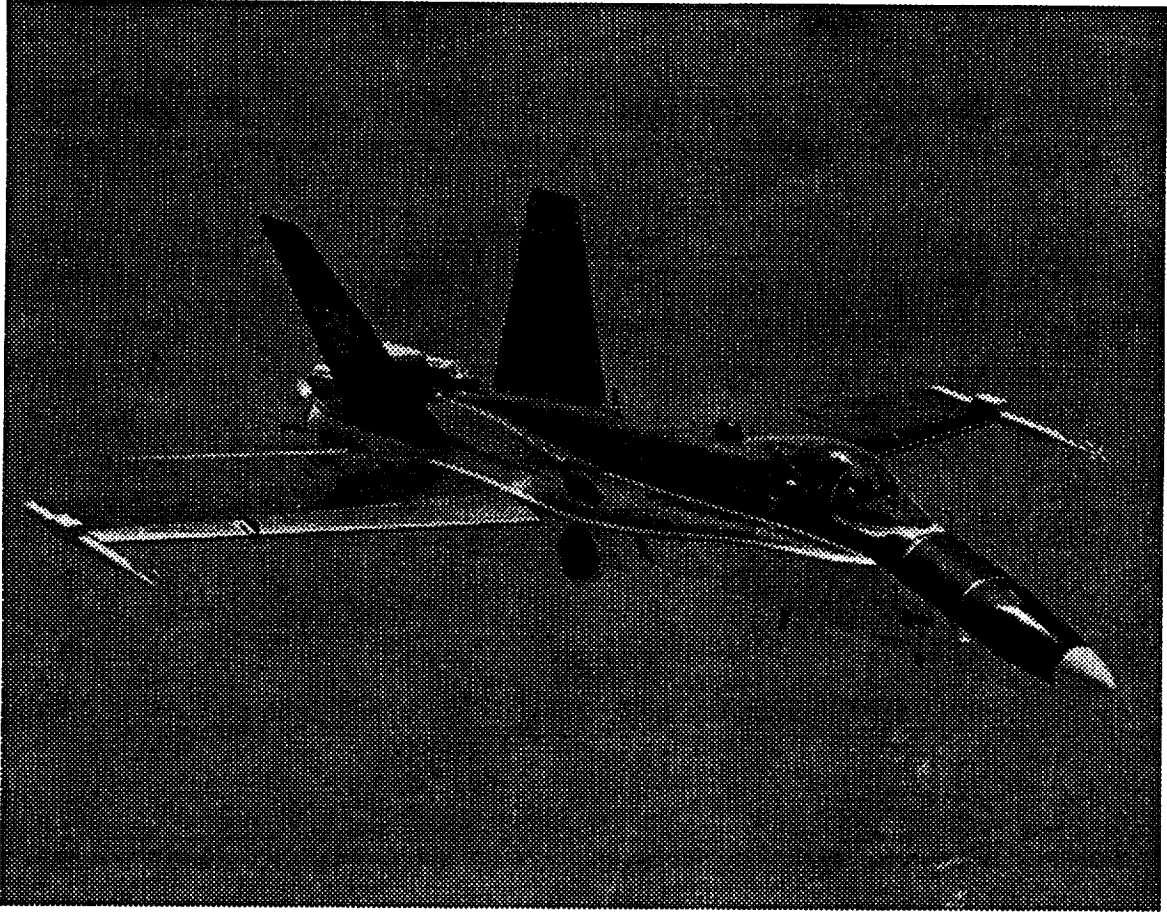
Fig. 1. F–18 HARV during flight tests.
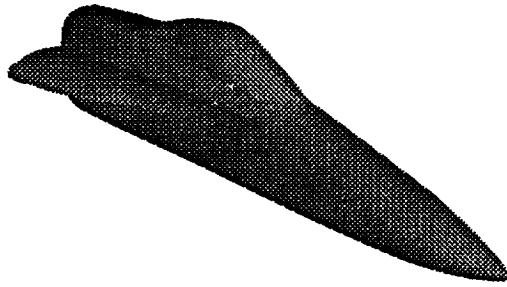
a) Isolated forebody and LEX (Ref. 8)
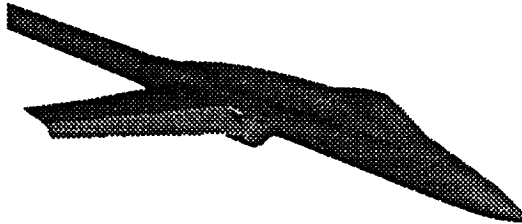
b) Fuselage and wing with deflected flap (Ref. 10)
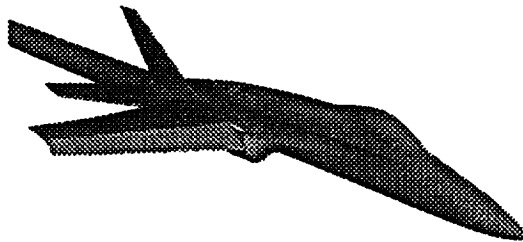
a) Near-complete geometry (Ref. 11)

Fig. 2. Progression of F–18 HARV geometry modeling.

····· Isolated Forebody/LEX (Ref. 8)
− − − Forebody/LEX and wing (Ref. 10)
−−− Complete Geometry (Ref. 11)
● Flight right (Ref. 12)
o Flight left (Ref. 12)
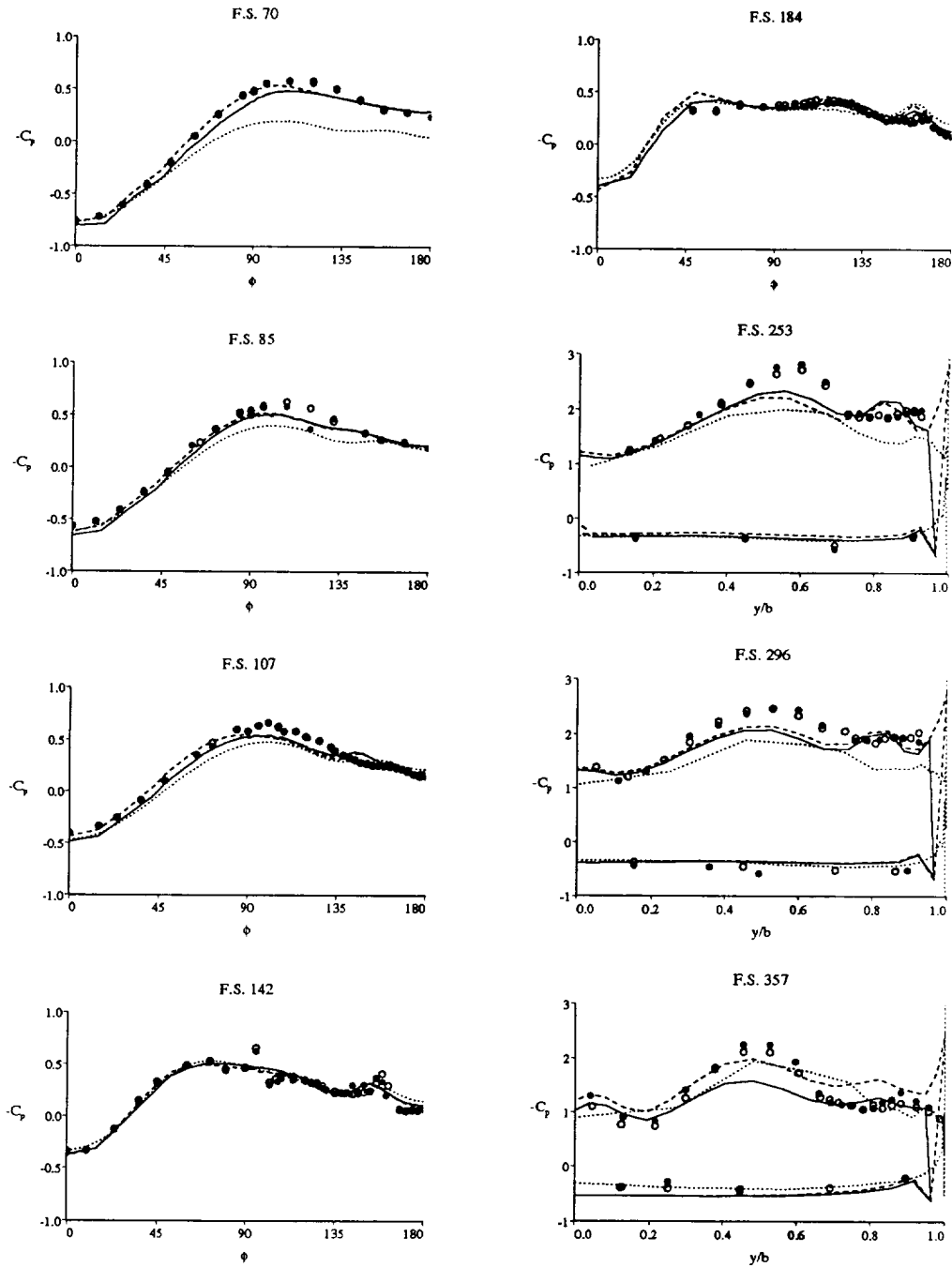
Fig. 3. Forebody and LEX pressure distribution ($\alpha = 30.3°$, $M_\infty = 0.243$, $Re_{\bar{c}} = 10.9 \times 10^6$).
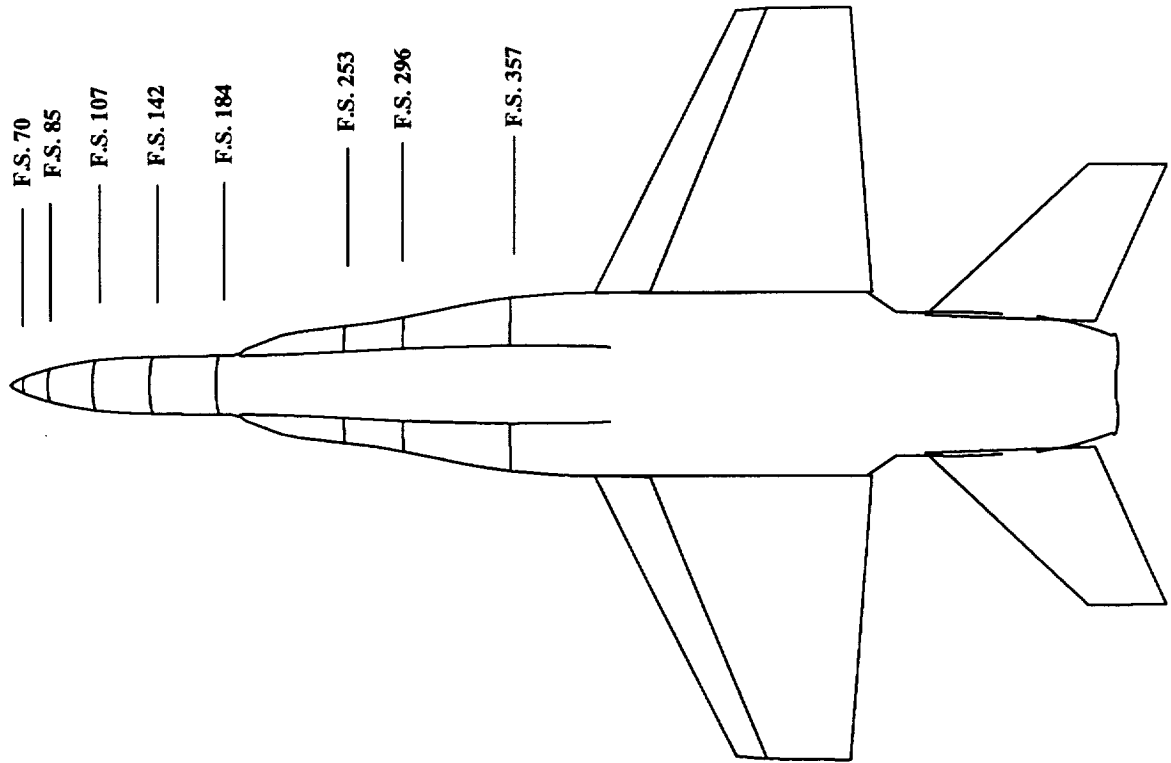
Fig. 4. F-18 HARV pressure-ring axial locations.
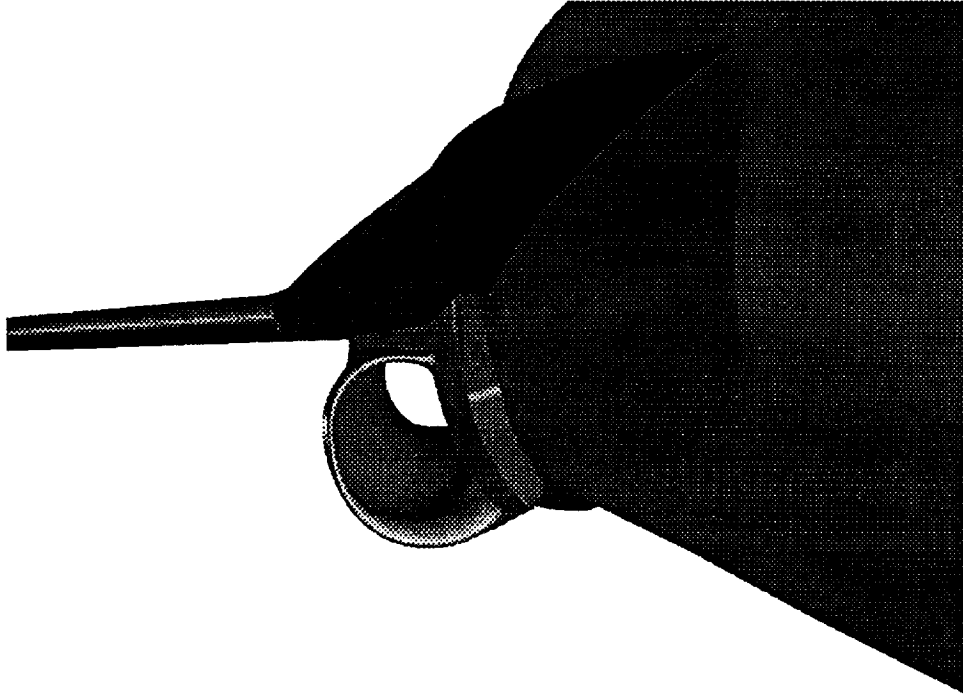
Fig. 5. Representation of F-18 HARV engine inlet geometry.

20
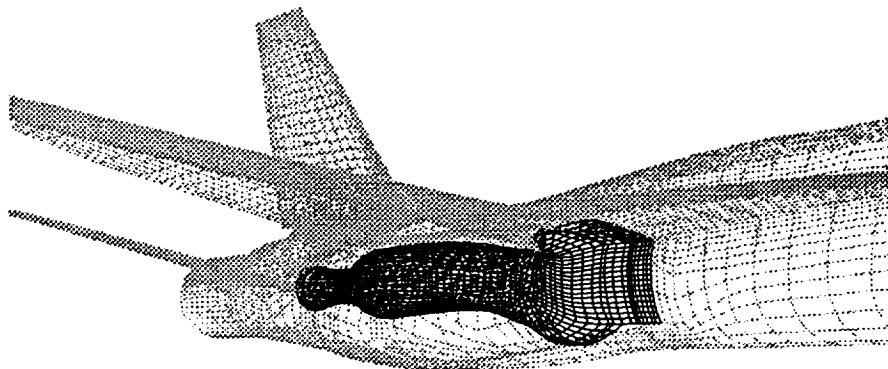
Fig. 6. Fuselage-diffuser surface definition.
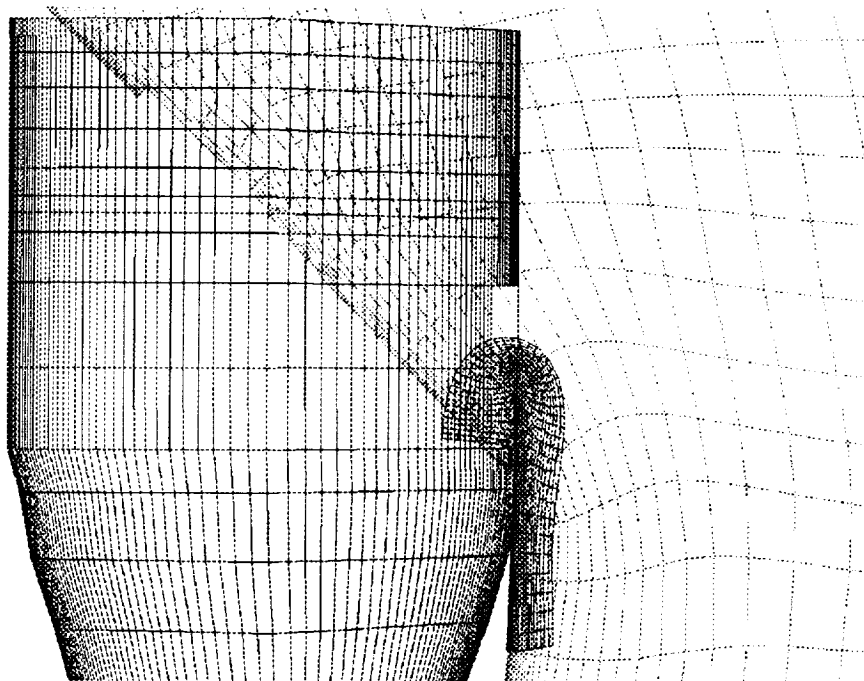
Fig. 7. Fuselage-diffuser-cowl grid interface.
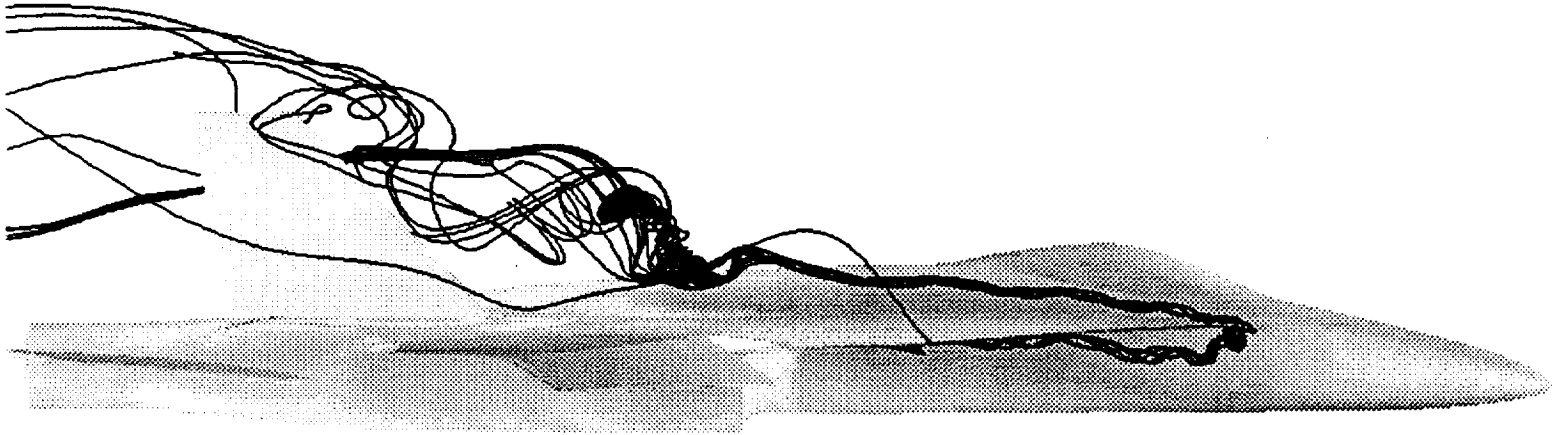
a) Faired-over inlet configuration
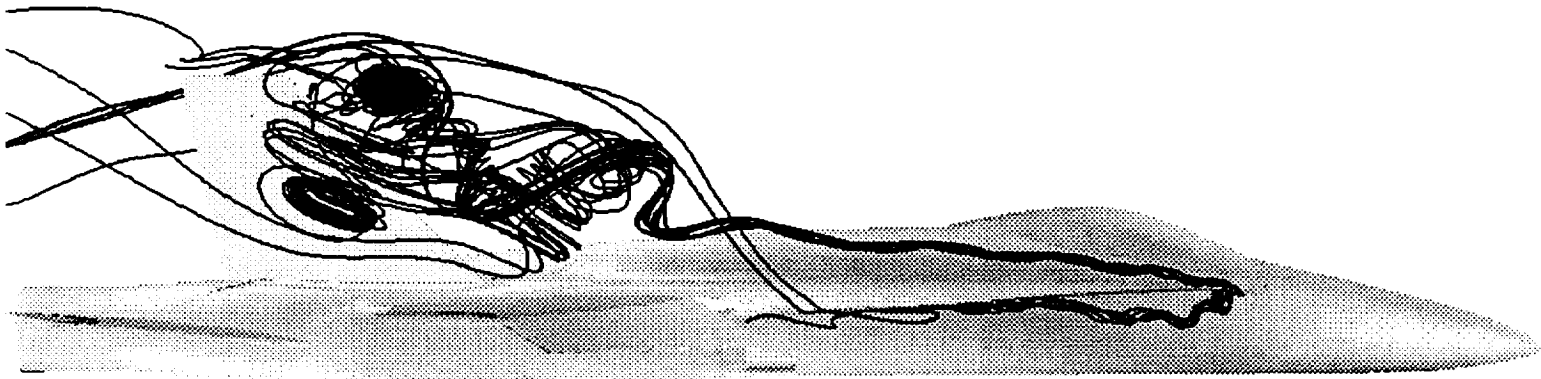
b) Flight-idle engine setting

a) Maximum power engine setting

Fig. 8. Computed particle streaklines around LEX ($\alpha = 30.3°$, $M_\infty = 0.243$, $Re_{\bar{c}} = 10.9$ x 10^6).

a) Flight-idle engine setting

b) Maximum power engine setting

Fig. 9. In-flight smoke flow visualization of LEX vortex at $\alpha = 25.0°$ (Ref. 14).
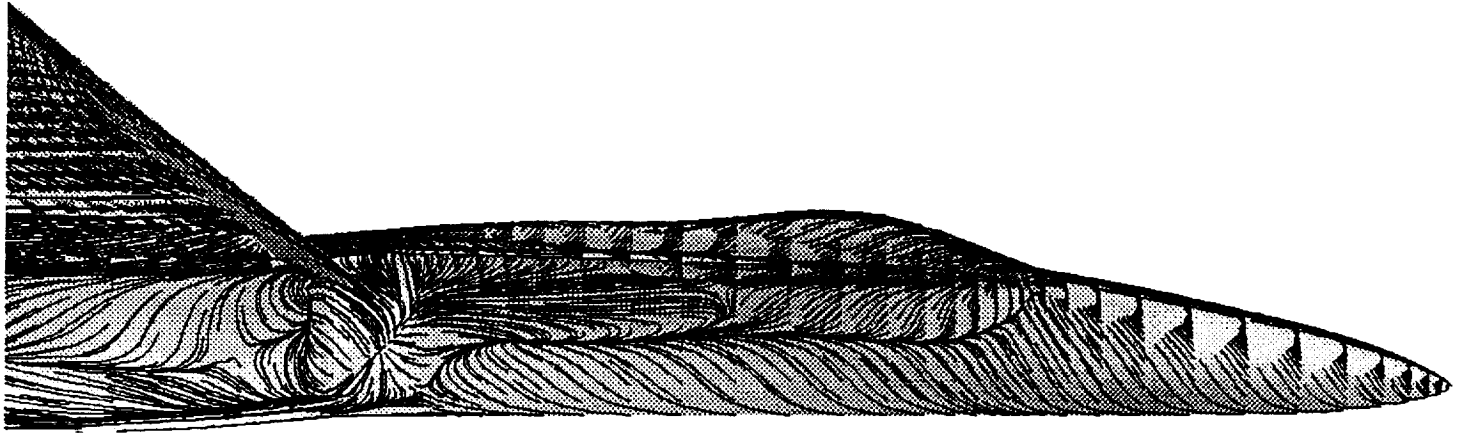
a) Faired-over inlet configuration
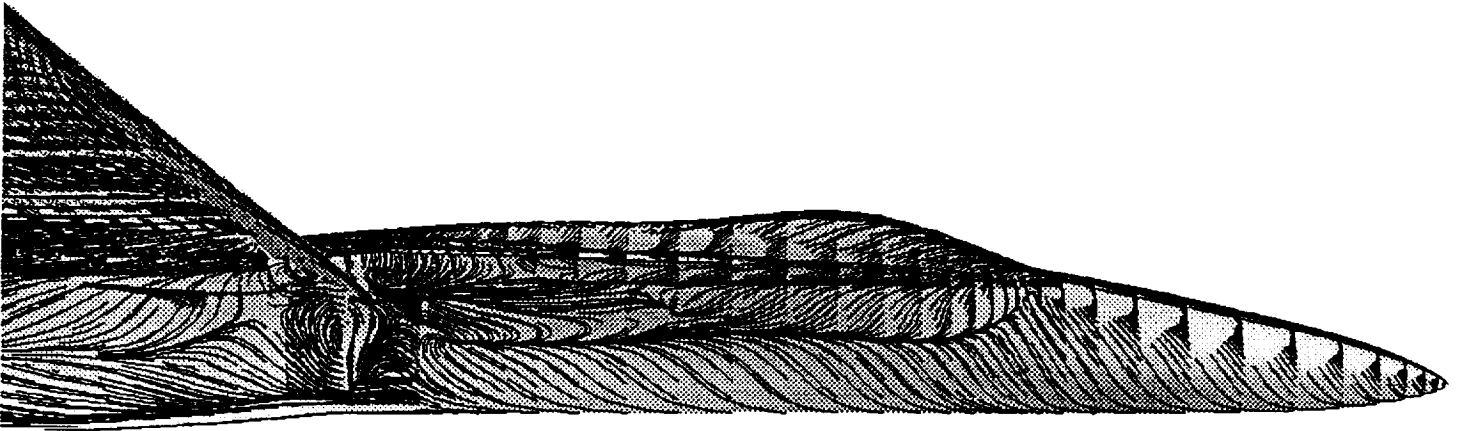
b) Flight-idle engine setting
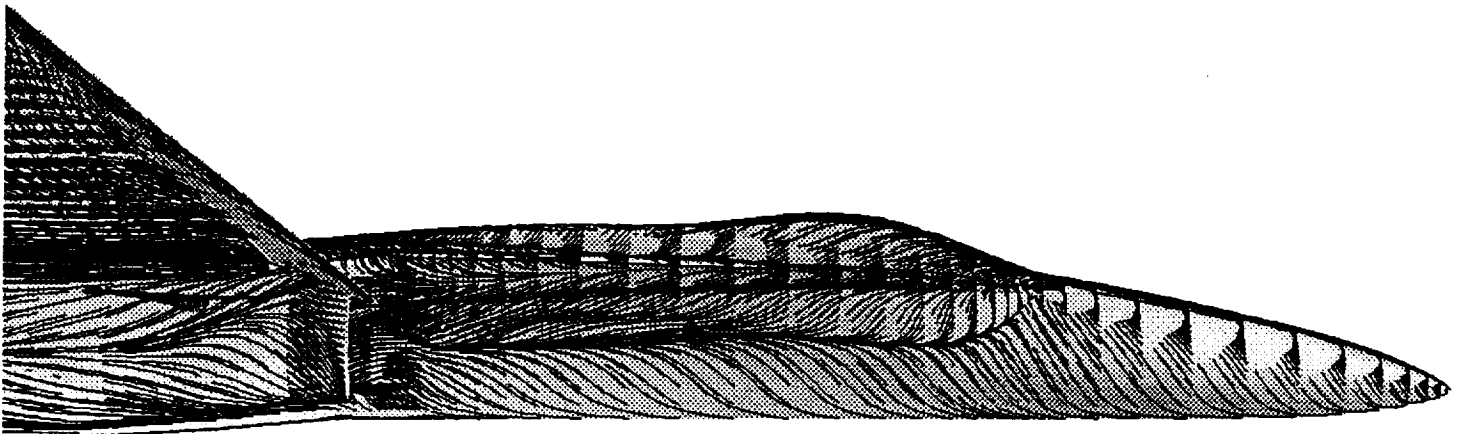
a) Maximum power engine setting

Fig. 10. Computed surface flow pattern ($\alpha = 30.3°$, $M_\infty = 0.243$, $Re_{\bar{c}} = 10.9$ x 10^6).
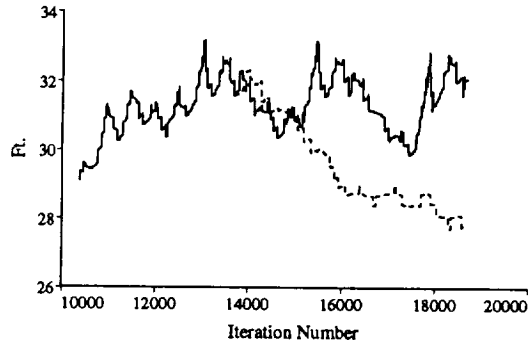
Fig. 11. Computed vortex breakdown position ($\alpha = 30.3°$, $M_\infty = 0.243$, $Re_{\bar{\varepsilon}} = 10.9$ x 10^6).
——— Non-time-accurate computation, - - - Time-accurate computation
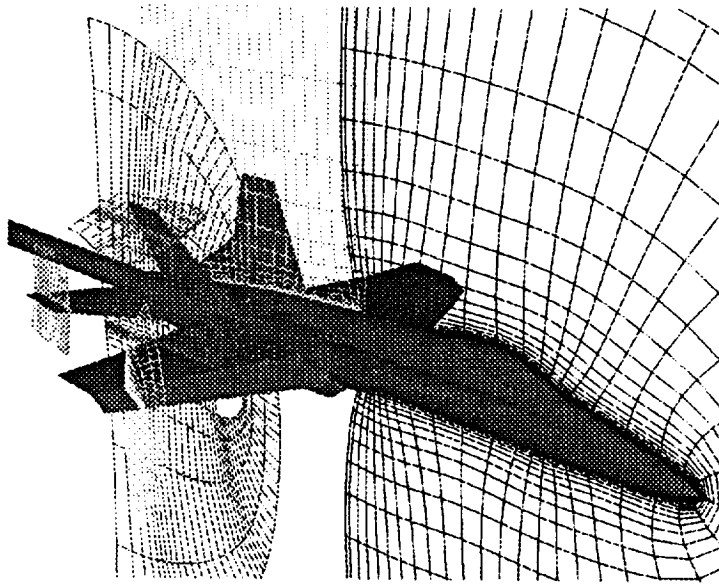
Fig. 12. Overview of F–18 HARV computational grid system
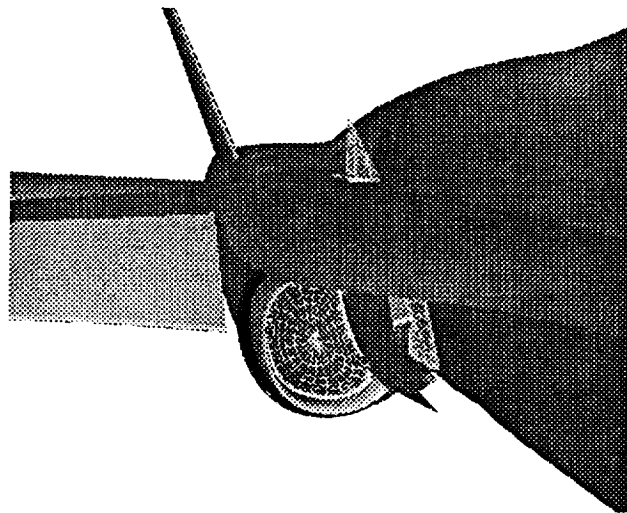
Fig. 13. Close-up view of engine inlet region.

25

Fig. 14. Forebody and LEX pressure distribution ($\alpha = 30.3°$, $M_\infty = 0.243$, $Re_{\bar{c}} = 10.9 \times 10^6$).

a) Flight-test oil-flow visualization (Ref. 19)
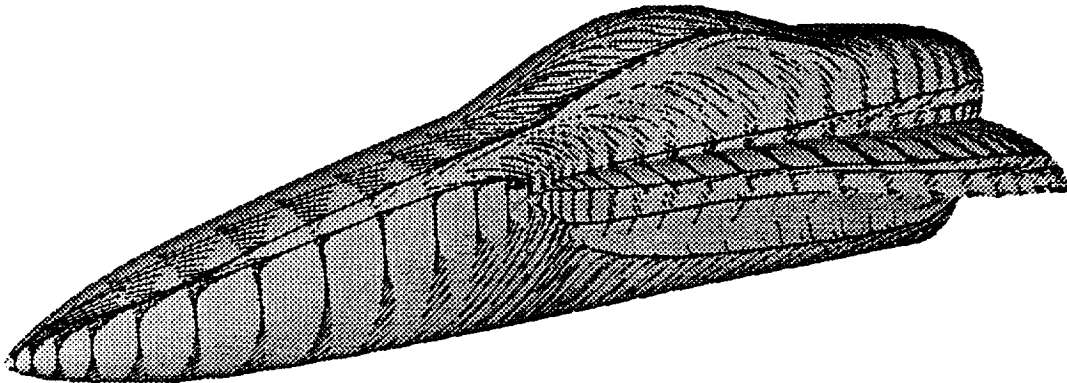
b) Coarse-grid computation
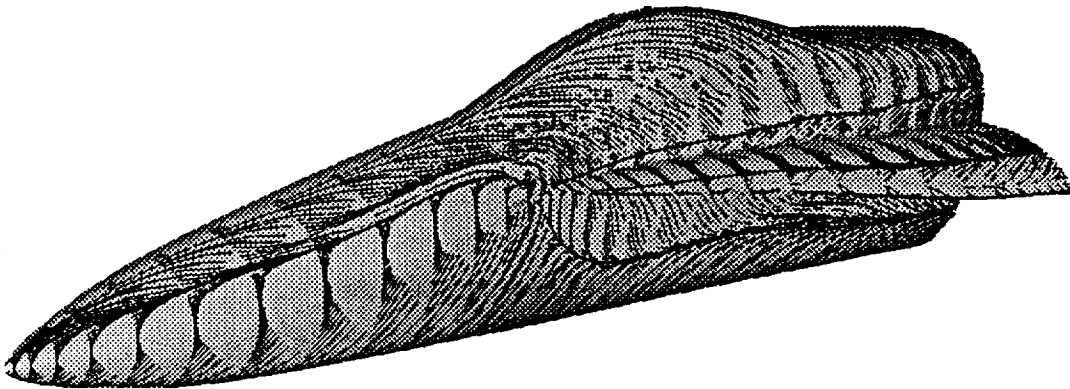
c) Fine-grid computation

Fig. 15. F–18 fuselage forebody surface flow pattern ($\alpha = 30.3°$, $M_\infty = 0.243$, $Re_{\tilde{z}} = 10.9 \times 10^6$).

27
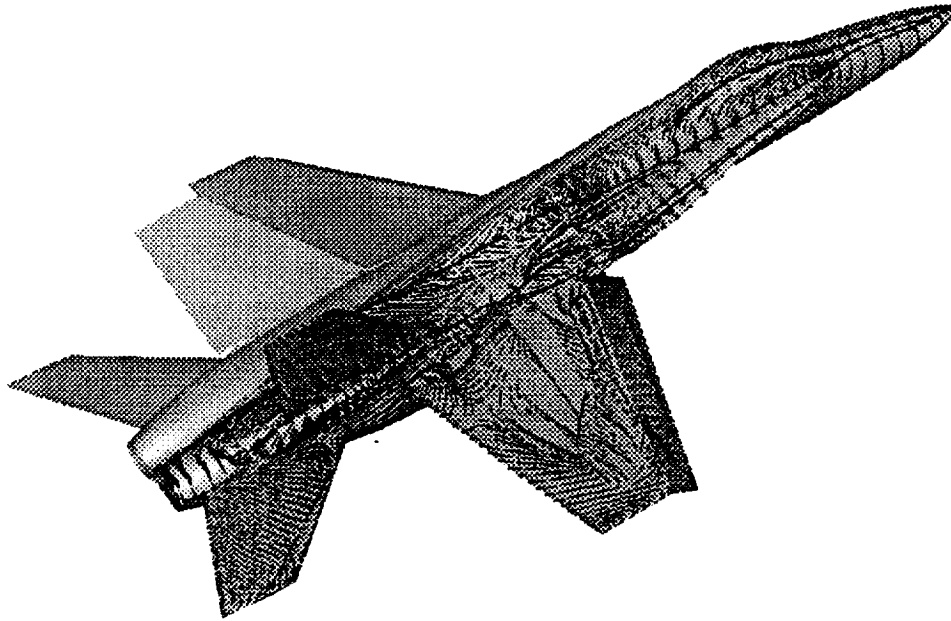
Fig. 16. Instantaneous surface streaklines ($\alpha = 30.3^\circ$, $M_\infty = 0.243$, $Re_{\bar{c}} = 10.9$ x 10^6).
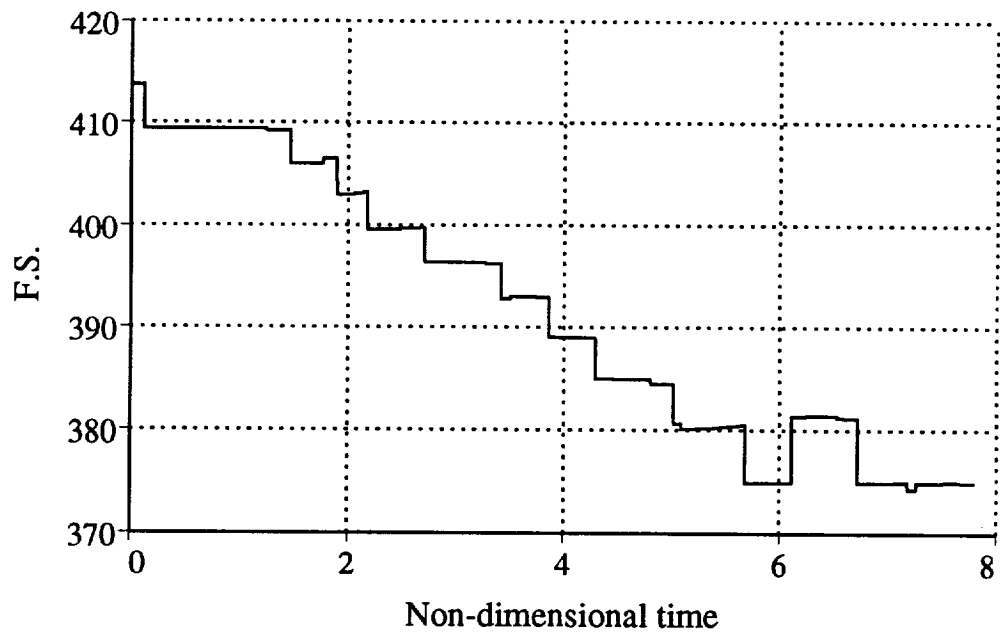
Fig. 17. Computed history of vortex breakdown position ($\alpha = 30.3^\circ$, $M_\infty = 0.243$, $Re_{\bar{c}} = 10.9$ x 10^6).
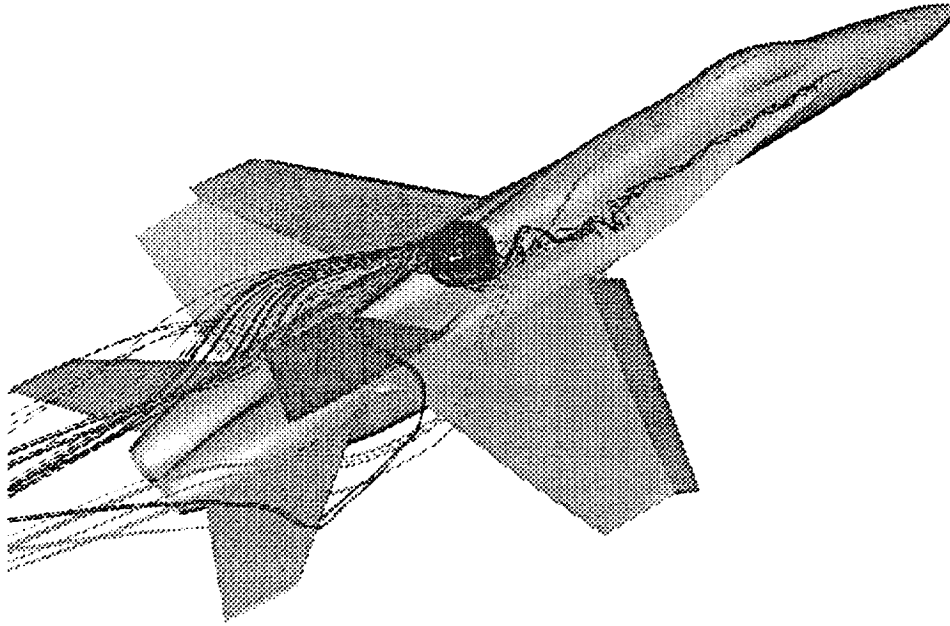
a) Fine-grid computation
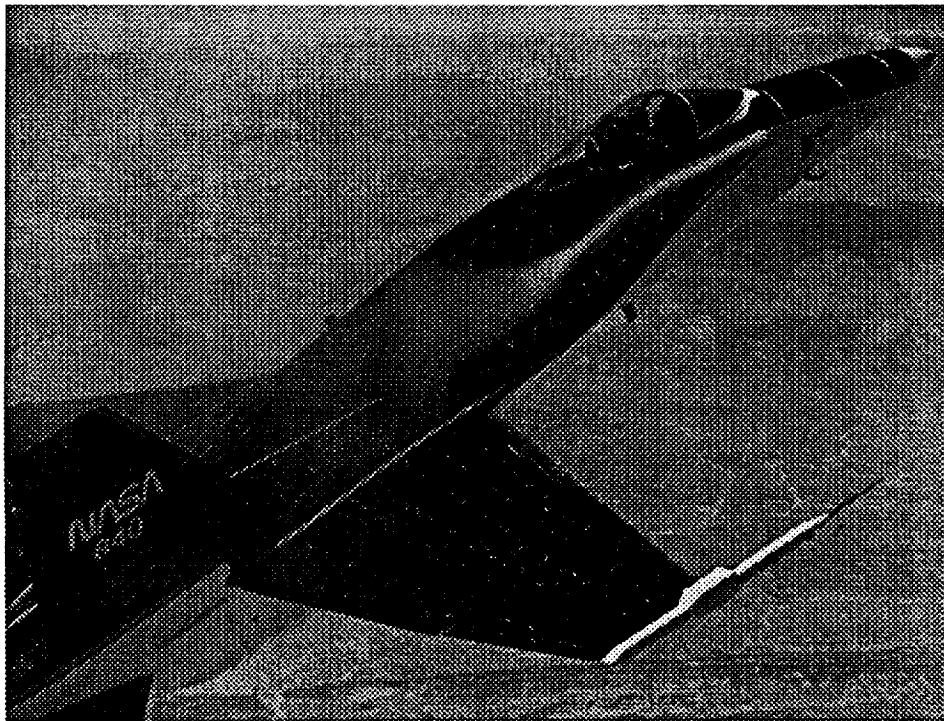
b) Flight-test smoke visualization (Ref. 19)

Fig. 18. F–18 vortex particle trajectories ($\alpha = 30.3°$, $M_\infty = 0.243$, $Re_{\bar{c}} = 10.9$ x 10^6).

o Fine-grid computation
⊕ Coarse-grid computation
• Flight data (Ref. 13)
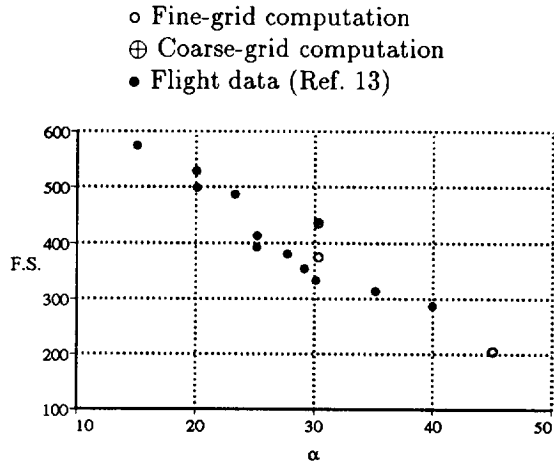
Fig. 19. Vortex breakdown position.

—— Computation
• Flight with natural transition (Ref. 20)
o Flight with forced transition (Ref. 20)
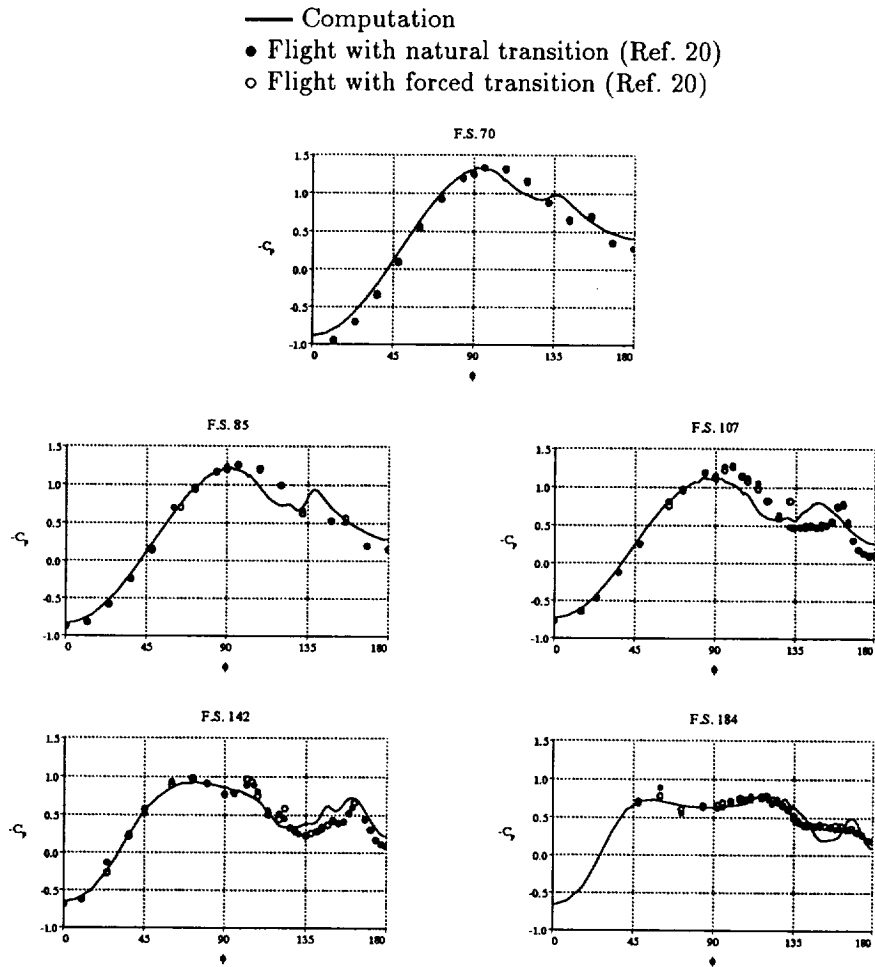
**Fig. 20.** Forebody pressure distribution ($\alpha = 44.7°$, $M_\infty = 0.258$, $Re_{\bar{c}} = 9.43$ x 10^6).

30
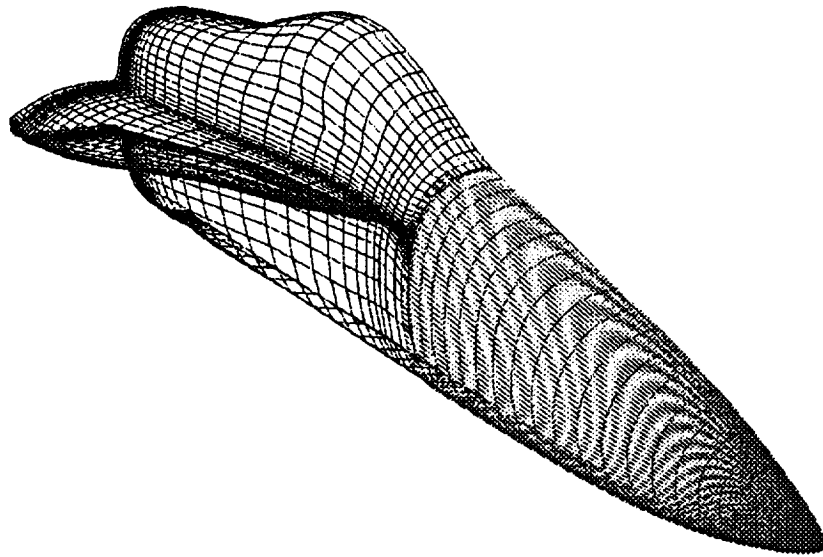
a) Modified two-zone fuselage forebody
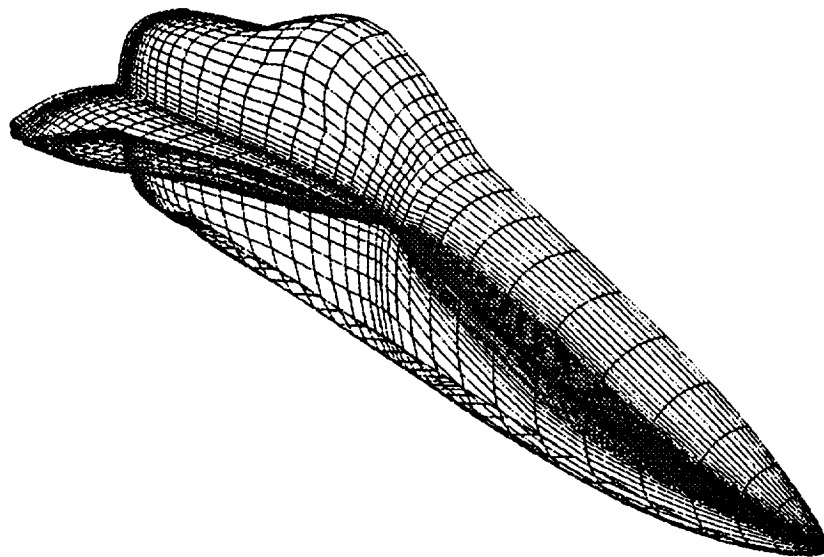
a) Original one-zone fuselage forebody

Fig. 21. Surface grid distributions for the $\alpha = 45°$ calculations.
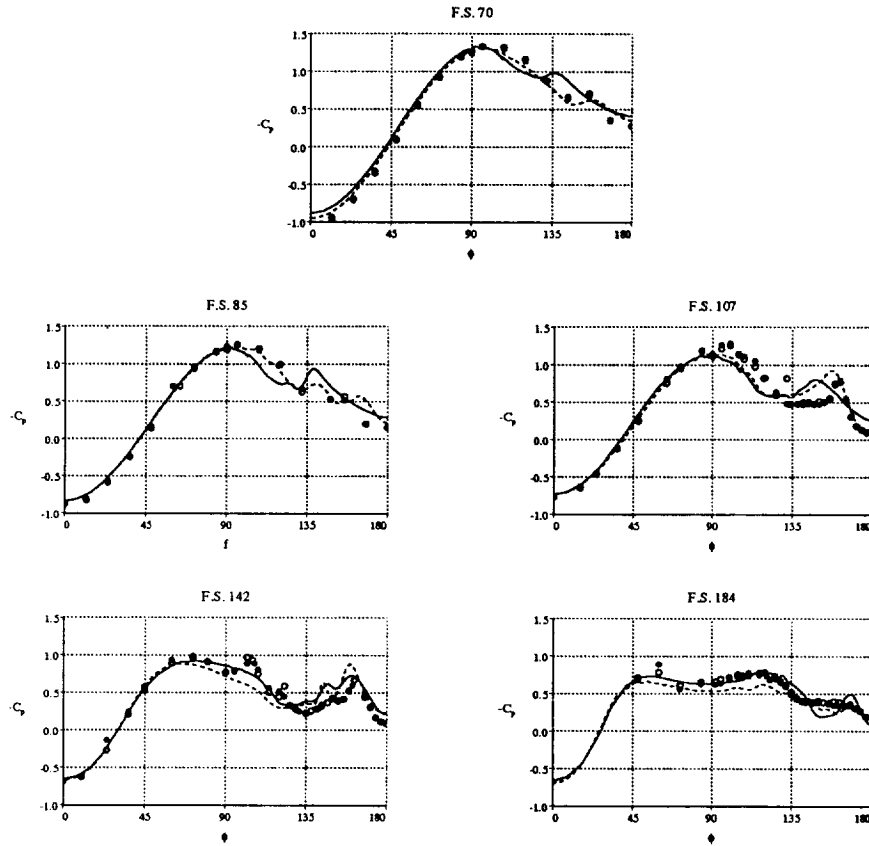
Fig. 22. Forebody pressure distribution ($\alpha = 44.7°, M_\infty = 0.258, Re_{\bar{c}} = 9.43 \times 10^6$).

32
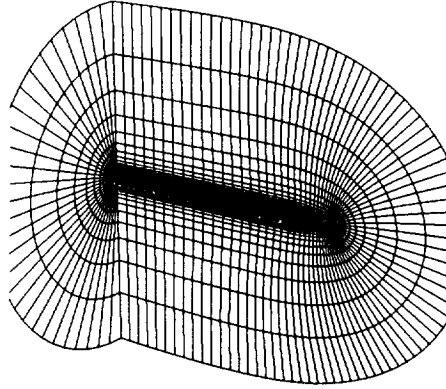
Fig. 23. Tangent-ogive cylinder grid configuration.
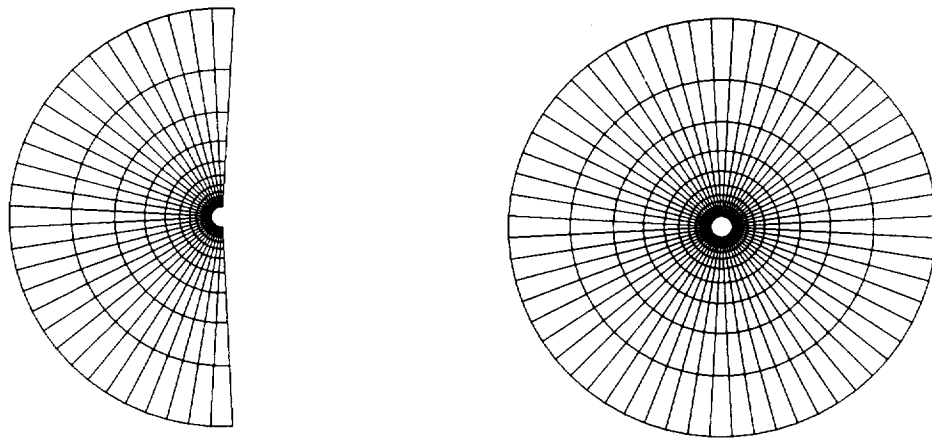
a. Lateral plane of symmetry.

b. Periodic grid.

Fig. 24. Symmetric grid boundary conditions.

Non-dimensional time
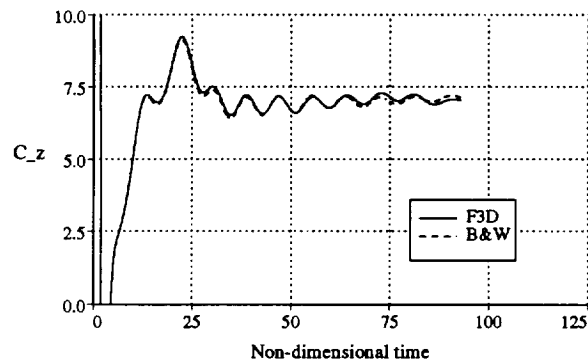
Fig. 25. Normal force history at $\alpha = 40°$, $Re_D = 80,000$.

33
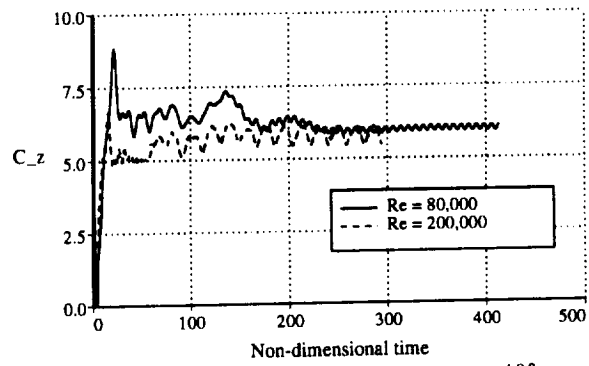
Fig. 26. Normal force history at $\alpha = 40°$.
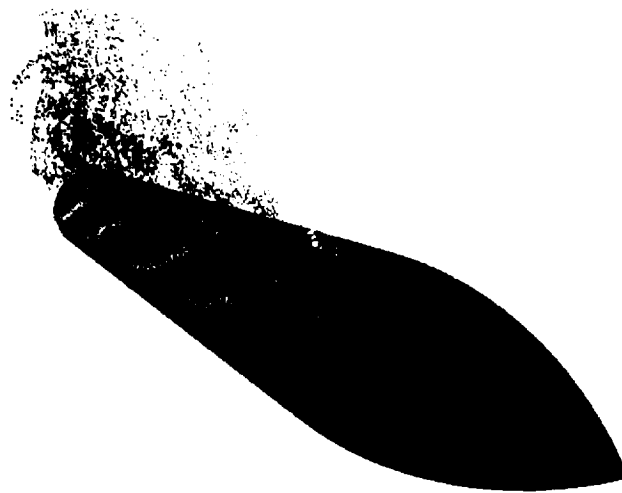
**Fig. 27.** Shear-layer shedding at $\alpha = 40°$, $Re_D = 200,000$.
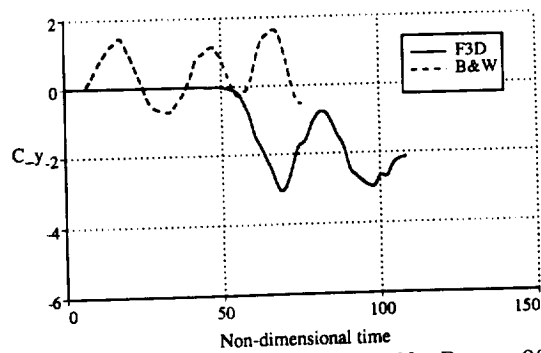
Fig. 28. Lateral force history at $\alpha = 60°$, $Re_D = 200,000$.